

An Airborne Thermal Imaging Methodology for Mapping Land Surface Temperature (LST) with a High Spatiotemporal Resolution

Ryan Byerlay¹, Mohammad Biglarbegan², Amir A. Aliabadi*

School of Engineering, University of Guelph, Guelph, Canada
rbyerlay@uoguelph.ca, mbiglarb@uoguelph.ca, [*aliabadi@uoguelph.ca](mailto:aliabadi@uoguelph.ca)

Abstract—A novel airborne thermal imaging technique is developed to map Land Surface Temperature (LST) with a high spatiotemporal resolution. A thermal camera is utilized as flown from a platform levitated by a tethered balloon. The developed method is suitable for near field observations with oblique view angles of the surrounding surface. In comparison to satellite observations, our approach results in less than 6% relative errors with a median relative error of 1.1% in predicting LST as compared to LST from images captured with the Moderate Resolution Imaging Spectroradiometer (MODIS).

Keywords—component; Georeferencing; Land Surface Temperature (LST); Airborne Thermal Imaging;

I. INTRODUCTION

Unmanned Aerial Vehicles (UAVs) and other airborne imaging platforms have become commonly used tools for remote sensing [1]. A remote sensing parameter of significant interest for atmospheric modeling, meteorology, and climatology is the spatial distribution of Land Surface Temperature (LST) [2]. Sources of LST commonly include sensors located on satellites such as Landsat 8, which carries the Thermal Infrared Sensor (TIRS) and Terra¹ and Aqua² which carry the Moderate Resolution Imaging Spectroradiometer (MODIS) sensor [3]. However, satellite LST data can be missing due to a variety of factors including cloud cover and sensor failure [4]. Furthermore, high spatial resolution LST data from satellites, such as Landsat 8³, is available at a low temporal resolution [5, 6]. Conversely, high temporal resolution LST data from satellite sensors, such as the Advanced Baseline Imager (ABI) on the Geostationary Operational Environmental Satellites R series of satellites (GOES-R)⁴, is available at a low spatial resolution [6]. That is, satellite-based sensors either offer high temporal – low spatial or low temporal – high spatial resolutions of LST. Recent advancements in both UAV and thermal imaging technologies have created opportunities for environmental LST to be accurately measured at a high spatiotemporal resolution. On-board UAV imaging systems, Global Positioning System (GPS) and Inertial Measurement Unit (IMU) data can be correlated to directly georeference image pixels to GPS coordinates without the use of Ground Control Points (GCPs) [7]. Coupling thermal imagery with common meteorological instruments to monitor environmental turbulent statistics on a UAV makes it possible to evaluate vertical heat fluxes among other meteorological data. Quantitative measurements of thermal imagery commonly utilize proprietary

software packages including PhotoScan Professional [8, 9], Pix4Dmapper [10] and MATLAB. Open source thermal image processing software such as Thermimage was developed for thermal image analysis⁵. However, open source thermal image processing coupled with integrated direct georeferencing of pixels is not widely distributed.

A Python based thermal image processing methodology was developed by the authors to calculate LST and to directly georeference images collected during a May 2018 field campaign for a remote northern mining location in Canada. The developed image processing methodology calculates georeferenced LST in decimal degrees of latitude and longitude. In this paper, we compare the results from the May 2018 campaign with respect to MODIS daytime LST at 1-kilometer horizontal spatial resolution. Percent relative error of LST was calculated between the method and the median of the MOD11A1⁶ data product, recorded on-board the Terra satellite, for each day from May 2018. The rest of the paper is organized as follows: Section II presents the data collection methodology and Python program development, Section III presents the LST results from the field campaign derived by the method and relative comparison to MODIS, Section IV discusses LST spatial patterns and relative errors of LST, and finally Section V concludes the paper.

II. MATERIALS AND METHODS

A. Field Campaign

During May 2018, the Tethered And Navigated Air Blimp 2 (TANAB2) completed multiple near surface profile measurements of the atmosphere. Thermal images were also collected using an uncooled FLIR Zenmuse XT 19-millimeter lens thermal camera. The camera was controlled by a DJI N3 Flight Controller and a DJI Lightbridge2 from either an Android or iOS device attached to the Lightbridge2. Wind velocities in the x, y and z directions, air pressure, and air temperature were also recorded from an onboard TriSonica Mini Ultrasonic Anemometer at 10Hz. All these components were attached to an aluminum structure and frame referred to as the gondola of the TANAB2.

One surface profile included the launching of the TANAB2 from grade level and a controlled release of line attaching the blimp to a fixed location at the surface of the Earth. Depending on environmental wind conditions, multiple mooring lines can be used and controlled by personnel. Utilizing three mooring lines, the TANAB2 was deployed in conditions with a maximum

¹ <https://terra.nasa.gov/about>

² <https://aqua.nasa.gov/>

³ <https://landsat.usgs.gov/what-are-band-designations-landsat-satellites>

⁴ <https://www.goes-r.gov/spacesegment/abi.html>

⁵ <https://github.com/gtatters/Thermimage>

⁶ https://lpdaac.usgs.gov/dataset_discovery/modis/modis_products_table/mod11a1_v006

wind speed of 10 meters per second. During ascent, images were collected by utilizing the Android or iOS device in conjunction with the Lightbridge2 to pan the thermal camera vertically and horizontally. Images were recorded up to a maximum of approximately 150 meters above grade level. Between May 5, 2018 and May 31, 2018, 11682 thermal images, each with a resolution of 640 pixels by 512 pixels were recorded.

B. Methodology

An image processing program utilizing Python, and associated open source image processing software, was developed on Ubuntu 16.04. Two additional open source software tools were used to extract information associated with the image metadata and camera signal values. These programs are ExifTool⁷ and ImageMagick respectively. Both programs were executed through the Linux terminal from the Python script and the outputs of each respective program were saved to variables in the Python program.

ExifTool was used to extract physical camera constants and image specific information. Data recorded by the integrated GPS and IMU in the DJI N3 flight controller was saved in the metadata of each image. ExifTool uses image tags to extract data. The tags vary by the manufacturer of the camera. Image specific information extracted from each picture included the latitude and longitude of the gondola when the image was recorded, the camera gimbal roll degree, the camera gimbal yaw degree, the camera gimbal pitch degree, the gondola roll degree, the gondola pitch degree and the altitude of the gondola. The raw signal recorded by individual pixels were extracted through using both ExifTool and ImageMagick. ImageMagick specified individual pixels to be extracted from the raw signal data while the ExifTool extracted the raw thermal pixel data.

All images have a gimbal pitch angle greater than -2° and less than or equal to -76° , where the horizontal plane is assumed to be zero degrees with positive angles upward. The gimbal pitch represents the angle for the center of an image. As per manufacturer specifications, the camera's mechanical pitch range is 45° and -135° . Images with a gimbal pixel angle greater than -30° may introduce error to the LST calculation⁸. Many images were recorded with oblique gimbal pitch angles between -2° and -30° . Excluding images within this range would have significantly reduced the spatial distribution of LST, such that spatial temperature gradients within the mining facility would have been omitted. Any top image pixels with a pitch angle greater than -1° at the top of each image (gimbal pitch angle plus half of the vertical field of view (VFOV) (26°)) were disregarded. This filtering was needed so that only pixels pointing to the land surface are included in the LST calculations. With this assumption, the pixel row for the top of each image was calculated through a mathematical relationship discussed below and visualized in Fig. 1 and Fig. 2. Images with a pitch angle of less than -76° were omitted for georeferencing simplicity as the pitch angle for the bottom of each image would be equivalent to less than -90° otherwise.

The altitude of the TANAB2 gondola (camera) was calculated through deriving a mathematical relationship between the atmospheric pressures recorded by the TriSonica relative to the atmospheric pressure at the start of each launch. The land

surface elevations in the eight cardinal directions (north, north-east, east, south-east, south, south-west, west and north-west) 10 kilometers away from each TANAB2 launch location were determined with the Geocontext-Profiler⁹ and exported to separate text files. In Python, a polynomial was fitted to the elevation data for each direction. A linear relationship representing the line of sight for the center of the camera was derived. The intersection(s) of these two equations was calculated and the smallest real positive solution was used as the surface level elevation and horizontal distance away from the TANAB2.

The geographic coordinates for the top, center, and bottom midpoints as well as corners of each image were calculated through a variation of the Haversine formula as per Equations 1 and 2.

$$Lat_2 = \arcsin[\sin(Lat_1) \cos\left(\frac{HDist}{R}\right) + \cos(Lat_1) \sin\left(\frac{HDist}{R}\right) \cos(Yaw)] \quad (1)$$

$$Lon_2 = Lon_1 + \operatorname{atan}^2\left[\sin(Yaw) \sin\left(\frac{HDist}{R}\right) \cos(Lat_1), \cos\left(\frac{HDist}{R}\right) - \sin(Lat_1) \sin(Lat_2)\right] \quad (2)$$

Where Lat_2 and Lon_2 represent the calculated geographic coordinates, Lat_1 and Lon_1 represent the geographic coordinates recorded by the N3 when each image was captured (i.e. gondola's GPS coordinates), $HDist$ represents the surface level horizontal distance away from the TANAB2, R represents the equatorial radius of the Earth in kilometers¹⁰ and Yaw represents the heading of the camera gimbal in degrees from north positive clockwise. All angles and geographic coordinates were converted to radians before calculating the new geographic coordinates. When deriving the geographic coordinates for pixels on the edges of the images, the horizontal distance away from the TANAB2 was determined through considering half of the horizontal field of view (HFOV) (32°) with the known horizontal distance away for the top, center and bottom of each image, respectively. Using simple trigonometric relationships, the $HDist$ was determined. If geographic coordinates of pixels in the middle of the image were to be calculated, the $HDist_{Vertical}$ was required. Conversely, if geographic coordinates of pixels on either the left or right edges of each image were to be calculated, the $HDist_{Edge}$ was required. To calculate the geographic location of pixels within the image, a relation between geographic distance and image pixels was identified.

A mathematical relationship was derived to determine the new top pixel row and the geographic distance away from the TANAB2 with respect to image pixels. This relation is illustrated in Figs. 1 and 2. Angles based on the vertical and horizontal fields of view properties of the camera are used to georeference nine locations for each image recorded including the corners and midpoints for the top, center and bottom of each image, respectively.

⁷ <http://u88.n24.queensu.ca/exiftool/forum/index.php?topic=7116.0>

⁸ https://dl.djicdn.com/downloads/zenmuse_xt/en/sUAS_Radiometry_Technical_Note.pdf

⁹ <http://www.geocontext.org/publ/2010/04/profiler/en/>

¹⁰ <https://nssdc.gsfc.nasa.gov/planetary/factsheet/earthfact.html>

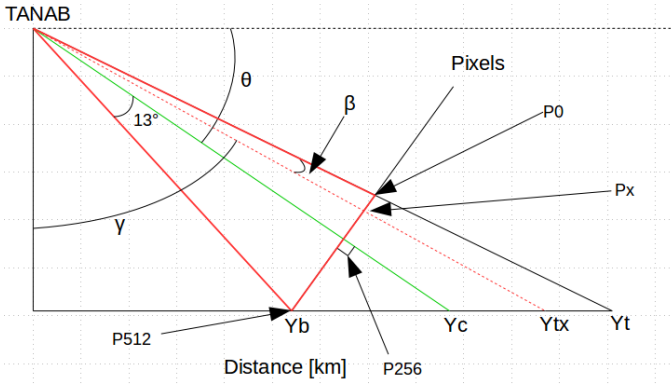


Figure 1. Relation between image pixels and horizontal distances.

Where Y_b , Y_c , Y_{tx} and Y_t represent the horizontal distance away from the TANAB2 for the bottom, center, new top and top of each image; P_0 , P_x , P_{256} and P_{512} represent the top pixel row, the new top pixel row, the center pixel row, and the bottom pixel row for each image, 13° is half of the VFOV, θ represents the pitch angle, γ and β represent angles used in equations that follow to correlate pixels to distances. The red triangle in Fig. 1 is displayed in more detail in Fig. 2.

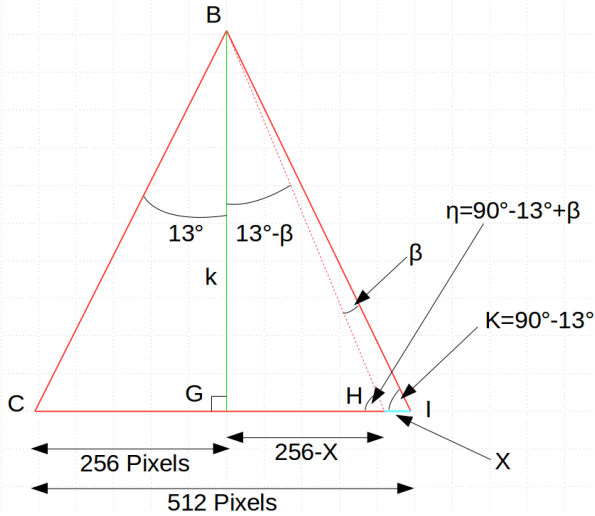


Figure 2. Relationship between VFOV and image pixels.

Where X represents the number of pixel rows omitted between the top of the image and another pixel row which itself is a function of the newly assigned top pitch angle. A geometric step function was used to determine the pixel steps for each row, where the majority of the pixel rows were located at the top of each image. In addition, every 64^{th} pixel across each column was selected and a corresponding geographic coordinate pair was calculated for each pixel column and row pair. At most each image would yield a maximum of 80 coordinate pairs. Most images yielded less as many images were assigned a new top pixel row. This pixel row (X) was calculated as a function of angles γ , β , κ and η as represented in the equations below

$$\gamma_{Dist-Pix} = \arctan\left(\frac{HDist_{vertical}}{Altitude}\right), \quad (3)$$

$$\beta_{Dist-Pix} = 90^\circ - \text{abs}(Gimbal\ Pitch) + 0.5 \cdot VFOV - \gamma_{Dist-Pix}, \quad (4)$$

$$\kappa = 90^\circ - 0.5 \cdot VFOV, \quad (5)$$

$$\eta = 90^\circ - 0.5 \cdot VFOV + \beta_{Dist-Pix}, \quad (6)$$

$$X_{Dist-Pix} = \frac{[0.5 \cdot VPR \cdot \sin(\beta)]}{[\sin(VFOV \cdot 0.5) \cdot \sin(180^\circ - \eta)]}, \quad (7)$$

where VPR is the Vertical Pixel Range and is 512 as per the camera specifications. For coordinates on the left and right edges of each image, the $HDist_{Edge}$ from the TANAB2 was calculated using Eq. 8

$$HDist_{Edge, Dist-Pix} = \frac{HDist_{vertical}}{\cos(0.5 \cdot HFOV)} \quad (8)$$

Using the same relationship as illustrated in Figs. 1 and 2, a set of equations were derived to relate numerical pixel locations to geographic distances. The relations described below were used when iterating through the pixel coordinates of an image. Rearranging Eq. 9, $\beta_{Pix-Dist}$ was solved for as shown in Eq. 10

$$\frac{\sin(0.5 \cdot VFOV)}{\sin(\kappa) \cdot [0.5 \cdot VPR]} = \frac{\sin(0.5 \cdot VFOV - \beta_{Pix-Dist})}{\sin(\eta) \cdot [0.5 \cdot VPR - j]}, \quad (9)$$

$$\beta_{Pix-Dist} = -\arctan\left(\frac{[0.5 \cdot VPR - j] \cdot \sin(0.5 \cdot VFOV)}{0.5 \cdot VPR \cdot \sin(\kappa)}\right) + 0.5 \cdot VFOV, \quad (10)$$

$$\gamma_{Pix-Dist} = 90^\circ - \text{abs}(Gimbal\ Pitch) + 0.5 \cdot VFOV - \beta_{Pix-Dist}, \quad (11)$$

$$Slope_{Pix-Dist} = \frac{-1}{\tan(\gamma_{Pix-Dist})}, \quad (12)$$

where j represents the vertical pixel row and $Slope_{Pix-Dist}$ represents the slope for the line of sight from the camera for each corresponding pixel location. The horizontal distance is derived using the same method described before using the data from Geocontext-Profiler. If georeferencing pixels between the edge and the center of an image, an angular offset based on the HFOV must be used when calculating the horizontal distance. This angular offset is directly related to the location of the pixel column with respect to the center of the image. Equations 1 and 2 were used to calculate the geographic coordinates for each pixel in an image. The angular offset was added or subtracted to the Yaw value depending on the location of the pixel column.

Using the raw signal value extracted from each pixel with ExifTool and ImageMagick in conjunction with heat transfer formulas based on Planck's Law, the LST was calculated. Martiny et al. [11] developed a partially empirical relationship

between Planck's Law (as described by Çengel and Ghajar [12] in Eq. 13) and the infrared pixel value recorded by a thermal camera (Eq. 14)

$$E_{b\lambda} = \frac{C_1}{\lambda^5 \cdot [\exp(\frac{C_2}{\lambda T}) - 1]}, \quad (13)$$

$$I = \frac{R}{\exp(\frac{B}{T}) - 1}, \quad (14)$$

where $E_{b\lambda}$ represents the emissive radiative power for a spectral black body, λ represents the wavelength of radiation released by the black body, T represents the surface temperature of the black body and C_1 and C_2 represent constants [12]. In Eq. 14, I represents the thermal radiation emitted from the imaged surface and T represents the temperature of the imaged surface. The remaining parameters represent constants which are directly influenced by the thermal camera and are determined during the calibration process by the camera manufacturer [11].

The total radiative energy recorded by a thermal camera as described by Usamentiaga et al. [13] and FLIR Systems [14] is a function of three radiative energy sources as per Eq. 15

$$U_{tot} = \varepsilon\tau U_{obj} + (1-\varepsilon)\tau U_{refl} + (1-\tau)U_{atm}, \quad (15)$$

where U_{tot} represents the total radiative energy recorded by a thermal camera, ε represents the emissivity of the imaged surface, τ represents the transmissivity of the atmosphere between the surface and the camera, U_{obj} represents the fraction of radiative energy emitted from the imaged surface, U_{refl} represents the theoretical fraction of radiative energy that is reflected from the imaged object based on an assumed reflective temperature and U_{atm} represents the radiative energy theoretically emitted from the atmosphere based on an assumed atmospheric temperature [14]. Usamentiaga et al. [13] noted that the transmissivity of the atmosphere is usually close to one, as a result, the atmospheric transmissivity was assumed to be equivalent to one. From the camera manufacturer, the apparent reflective temperature used to calculate the U_{refl} was 295.15 K. The U_{refl} term was calculated using the following equation

$$U_{refl} = \frac{R_1}{R_2 \cdot [\exp(\frac{B}{T_{refl}}) - F]} - O, \quad (16)$$

where R_1 , R_2 , B , F and O are all constants determined by the camera manufacturer. These constants in addition to the apparent reflective temperature were extracted from the metadata of each image with ExifTool.

The emissivity of the land surface was derived from a remote sensing satellite. MODIS imaged the land surface twice daily over the entire field campaign. Using the MOD11B3¹¹ data product, recorded from the Terra satellite, the average land surface emissivity at a spatial resolution of 6 kilometers for three specific spectral ranges over the entire study area was calculated. Wang et al. [15] developed a relationship to determine the Broadband Emissivity (BBE) as a function of the three spectral

bands recorded by MODIS. The BBE relation (Eq. 17) was used to calculate the land surface temperature from the thermal images.

$$BBE = a\varepsilon_{29} + b\varepsilon_{31} + c\varepsilon_{32}, \quad (17)$$

where ε_{29} , ε_{31} and ε_{32} are the spectral emissivity bands from MODIS (Bands 29, 31 and 32, respectively) and a , b and c are constants determined to be acceptable for soil, vegetation and anthropogenic land surfaces [15].

The radiative energy signal from the imaged object recorded by the thermal camera was calculated using Eq. 18 and the corresponding object surface temperature was calculated with Eq. 19

$$U_{obj} = \frac{U_{tot} - [(1-\varepsilon)U_{refl}]}{\varepsilon}, \quad (18)$$

$$T_{obj} = \frac{B}{\ln[\frac{R_1}{R_2(U_{obj}+O)}+F]}, \quad (19)$$

where ε is the BBE of a specific geographic location and T_{obj} is the LST of a specific geographic location.

III. RESULTS

The median LST values from the entire field campaign were calculated at a spatial resolution of 1-kilometer for six four-hour intervals in Local Daylight Time (e.g. 00:00-04:00 LDT, 04:00-08:00 LDT, 08:00-12:00 LDT, 12:00-16:00 LDT, 16:00-20:00 LDT, 20:00-24:00 LDT). Spatial distribution of LST with respect to important land surface features are included below. Geographically important land features include the perimeter of the facility (black), the perimeter of a tailings pond (blue), the perimeter of a mine (red), and the TANAB2 launch locations (white dots in Figs. 3 and 5). The temperature distribution of LST of both the tailings pond and mine for the corresponding four-hour intervals are represented as boxplots in Fig. 4.

A comparison of the median LST at 1-kilometer spatial resolution collected during May 24th was also completed with MODIS LST data from the MOD11A1 data product. The TANAB2 was deployed within the mine perimeter on this day, as denoted by the white dot within the mine perimeter in Fig. 5. The spatial distribution of percentage relative error between the two methods with respect to key land features is also presented.

IV. DISCUSSION

The spatial distribution and variation of LST varies diurnally as shown in Figs. 3 and 4. In general, the mine and areas around the mine are warmer as compared to other areas of the mining facility. The spatial distribution of LST within the mine and pond varies the least between 04:00 and 08:00 LDT. Between 00:00 and 04:00 there is a noted temperature gradient between the pond and the mine. This gradient is apparent for all other time periods except for the 04:00 to 08:00 LDT time period.

¹¹ https://lpdaac.usgs.gov/dataset_discovery/modis/modis_products_table/mod11b3_v006

The LST derived from images recorded from the May 24th, 2018 field campaign compared well with the MODIS LST as shown in Fig. 5. LST in and around the mine appear to have a percentage error of approximately 6% or less. Furthermore, the overall median relative error was determined to be 1.1%. Areas west and north-west of the mine have a higher percentage error which may be attributed to higher surface elevations as

compared to the mine itself and areas east of the mine. Temperatures at these pixels require very oblique view angles, i.e. pitch angles closer to the horizontal, therefore reduced accuracy due to solar reflection and a thick atmospheric boundary layer, through which the image quality may be disrupted.

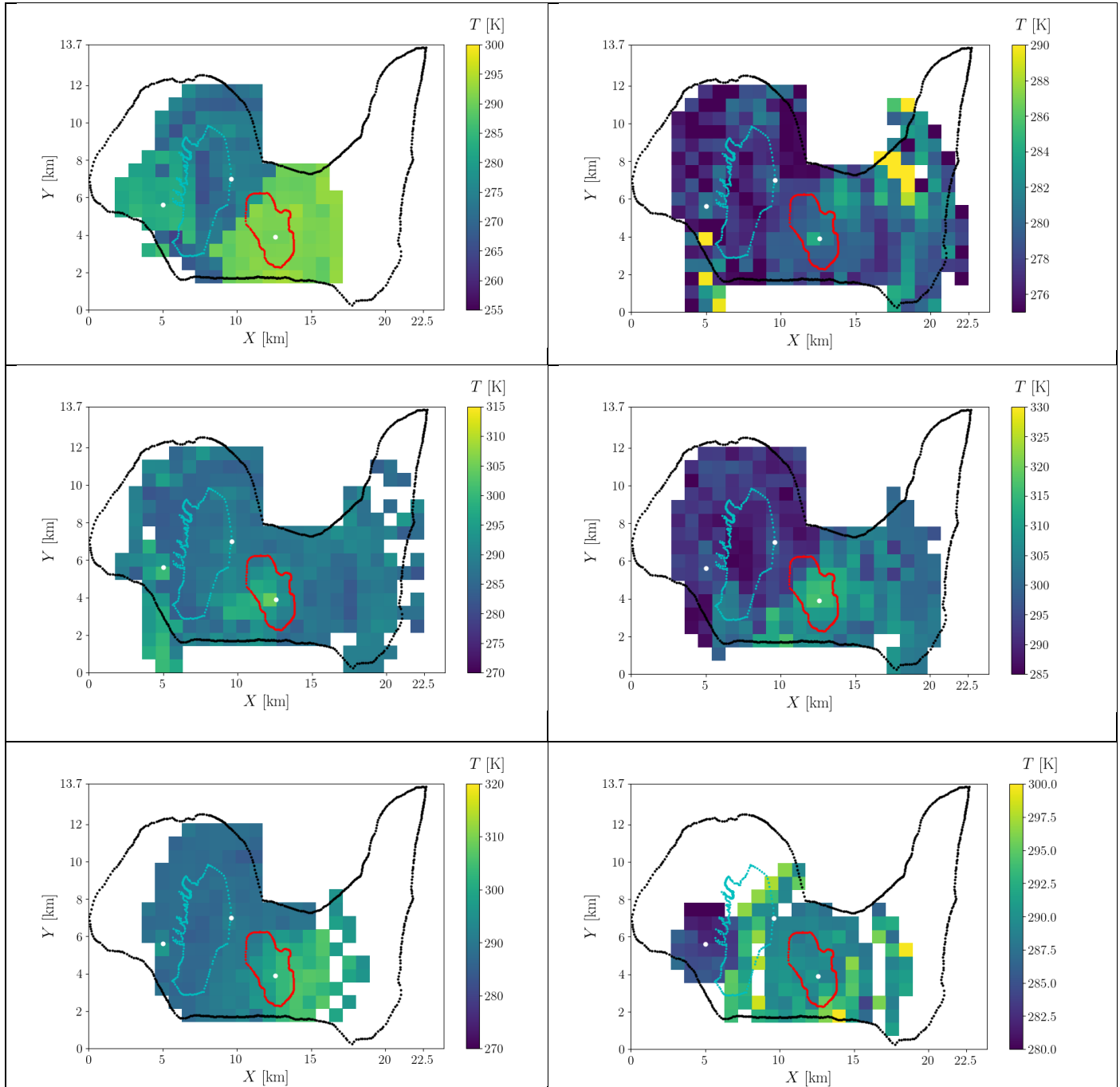


Figure 3. Median temperatures at 00:00 – 04:00 LDT (top left), 04:00-08:00 LDT (top right), 08:00-12:00 LDT (middle left), 12:00-16:00 LDT (middle right), 16:00-20:00 LDT (bottom left), 20:00-24:00 LDT (bottom right); at 1-km by 1-km horizontal spatial resolution.

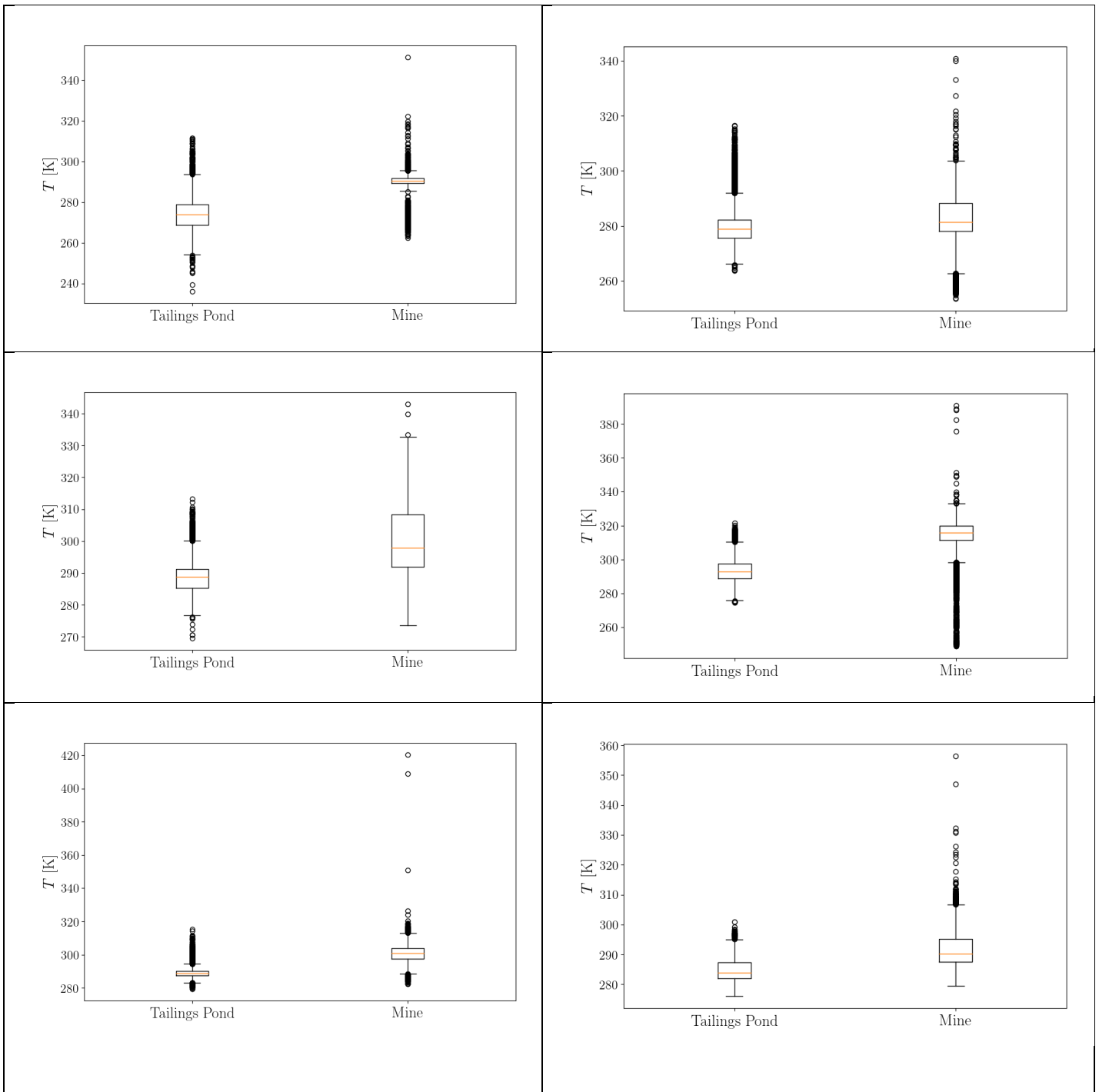


Figure 4. Boxplot of temperatures at 00:00-04:00 LDT (top left), 04:00-08:00 LDT (top right), 08:00-12:00 LDT (middle left), 12:00-16:00 LDT (middle right), 16:00-20:00 (bottom left), 20:00-24:00 LDT (bottom right); for tailings pond and mine.

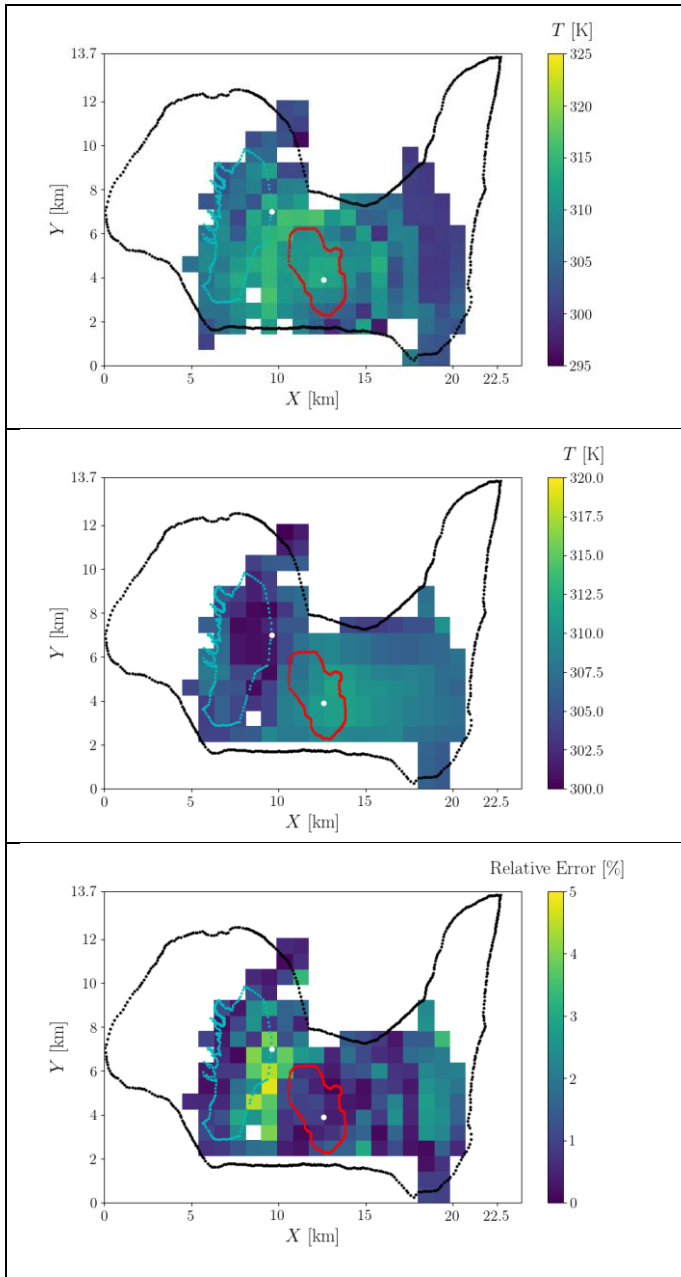


Figure 5. Median temperatures from May 24, 2018 12:00-14:00 LDT recorded from images captured by the thermal camera (top), daytime temperatures from the early afternoon on May 24, 2018 derived from the MODIS MOD11A1 data product (middle), percentage error between thermal camera and MODIS LST on May 24 (bottom).

In total, 98% of the total 11 682 images were processed with the method and LST from individual pixels were calculated. The number of images or pixels within an image processed with the method can be changed depending on the data set size and preferences of the user. The size of the image data set is much larger than any singular satellite image from Landsat 8 or GOES. However, with an image dataset, parameters within the methodology, can be adjusted to spatially represent LST with a very high spatial resolution over any specified time period.

Using satellite image datasets, these advantages cannot be realized due to inherent limitations of satellite sensors.

V. CONCLUSION

A novel airborne thermal imaging technique is developed to measure Land Surface Temperature (LST) with a high spatiotemporal resolution. A thermal camera is deployed on a tethered balloon in a remote mine field in northern Canada in May 2018. The terrain variability and camera's GPS position, altitude, pitch, and yaw angles were used to georeference each recorded pixel in the thermal image by tagging a latitude and longitude to it. The developed method was suitable for near field observations with moderately oblique view angles of the surrounding surface. In comparison to MODIS satellite observations, our method results in less than 6% relative errors in predicting LST close to the launch. This error increases with pitch angles closer to the horizontal. Our approach provides high spatial and temporal resolution of LST measurements simultaneously and therefore overcome limitations of satellites that cannot achieve both high spatial and temporal resolutions at the same time.

ACKNOWLEDGMENT

The airborne thermal imaging system was developed by the assistance of Denis Clement, Jason Dorssers, Katharine McNair, James Stock, Darian Vyriotes, Amanda Pinto, and Phillip Labarge. The authors thank the assistance of the following individuals in operating the thermal imaging system for the May 2018 campaign: Amir Nazem, Md. Rafsan Nahian, and Manoj Kizhakkeniyil. In-kind technical support for this work was provided by Rowan Williams Davies and Irwin Inc. (RWDI). This work was supported by the Discovery Grant program (401231) from the Natural Sciences and Engineering Research Council (NSERC) of Canada; Government of Ontario through the Ontario Centres of Excellence (OCE) under the Alberta-Ontario Innovation Program (AOIP) (053450); and Emission Reduction Alberta (ERA) (053498). OCE is a member of the Ontario Network of Entrepreneurs (ONE).

REFERENCES

- [1] Jose A. J. Berni, Pablo J. Zarco-Tejada, Lola Suárez, and Elias Fereres, "Thermal and Narrowband Multispectral Remote Sensing for Vegetation Monitoring From an Unmanned Aerial Vehicle," *IEEE Trans. Geosci. Remote Sens.*, 2009, 47(3):722-738.
- [2] Charlie J. Tomlinson, Lee Chapman, John E. Thornes, and Christopher Baker, "Remote sensing land surface temperature for meteorology and climatology: a review," *Meteorol. Appl.*, 2011, 18(3):296-306.
- [3] Estoque, Ronald C. and Murayama, Yuji, "Classification and change of built-up lands from Landsat-7 ETM+ and Landsat-8 OLI/TIRS imageries: A comparative assessment of various spectral indices," *Ecol. Indic.*, 2015, 56:205-217.
- [4] Hamid Reza Ghafarian Malamiri, Iman Roustaa, Haraldur Olafsson, Hadi Zare, and Hao Zhang, "Gap-Filling of MODIS Time Series Land Surface Temperature (LST) Products Using Singular Spectrum Analysis (SSA)," *Atmosphere-Basel*, 2018, 9(9):334.
- [5] Panagiotis Sismanidis, Iphigenia Keramitsoglou, and Chris T. Kiranoudis, "Diurnal Analysis of Surface Urban Heat Island Using Spatially Enhanced Satellite derived LST Data," *Joint Urban Remote Sensing Event*, June 2015, Lausanne.

- [6] Klemen Zakšek and Kristof Oštir, "Downscaling land surface temperature for urban heat island diurnal cycle analysis," *Remote Sens. Environ.*, 2012, 117:114-124.
- [7] Darren Turner, Arko Lucieer, and Luke Wallace, "Direct Georeferencing of Ultrahigh-Resolution UAV Imagery," *IEEE Trans. Geosci. Remote Sens.*, 2014, 52(5):2738-2745
- [8] Yoann Malbêteau, Stephen Parkes, Bruno Aragon, Jorge Rosas, and Matthew F. McCabe, "Capturing the Diurnal Cycle of Land Surface Temperature Using an Unmanned Aerial Vehicle," *Remote Sens.*, 2018, 10(9):1407.
- [9] H. Hoffmann, H. Nieto, R. Jensen, R. Guzinski, P. Zarco-Tejada, and T. Friborg, "Estimating evaporation with thermal UAV data and two-source energy balance models," *Hydrol. Earth Syst. Sci.*, 2016, 20(2): 697-713.
- [10] Abdul Nishar, Steve Richards, Dan Breen, John Robertson, and Barbara Breen, "Thermal infrared imaging of geothermal environments and by an unmanned aerial vehicle (UAV): A case study of the Wairakei- Tauhara geothermal field, Taupo, New Zealand," *Renew. Energ.*, 2016, 86:1256-1264.
- [11] M. Martiny, R. Schiele, M. Gritsch, A. Schulz, and S. Wittig, "In Situ Calibration for Quantitative Infrared Thermography," *Quant. Infr. Therm. J.*, 1996.
- [12] Yunus A. Çengel and Afshin J. Ghajar, *Heat and Mass Transfer: Fundamentals and Applications*, 5th Edition. New York, NY: McGraw-Hill Education, 2015.
- [13] Rubén Usamentiaga, Pablo Venegas, Jon Guerediaga, Laura Vega, Julio Molleda, and Francisco G. Bulnes, "Infrared Thermography for Temperature Measurement and Non-Destructive Testing," *Sensors-Basel*, 2014, 14(7):12305-12348.
- [14] FLIR Systems, *Installation Manual: FLIR A3XX series FLIR A6XX series*, 2010.
- [15] Kaicun Wang, Zhengming Wan, Pucui Wang, Michael Sparrow, Jingmao Liu, Xiuji Zhou, and Shigenori Haginoya, "Estimation of surface long wave radiation and broadband emissivity using Moderate Resolution Spectroradiometer (MODIS) land surface temperature/emissivity products," *J. Geophys. Res.*, 2005, 110(D11).